

# Site-specific reactivity of molecules with surface defects - the case of H<sub>2</sub> dissociation on Pt

Richard van Lent,<sup>1,2</sup> Sabine V. Auras,<sup>1</sup> Kun Cao,<sup>1</sup> Anton J. Walsh,<sup>2</sup>  
Michael A. Gleeson,<sup>2</sup> Ludo B.F. Juurlink<sup>1\*</sup>

<sup>1</sup>Leiden Institute of Chemistry, Leiden University, Einsteinweg 55, 2333 CC Leiden, the Netherlands

<sup>2</sup>Dutch Institute for Fundamental Energy Research, de Zaale 20, 5612 AJ Eindhoven, the Netherlands

\*To whom correspondence should be addressed; E-mail: L.Juurlink@chem.leidenuniv.nl.

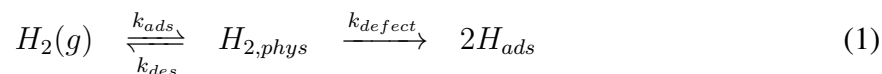
**The classic system that describes weakly activated dissociation in heterogeneous catalysis has been explained by two dynamical models that are fundamentally at odds. Whereas one model for hydrogen dissociation on Pt(111) invokes a pre-equilibrium and diffusion toward defects, the other is based on direct and localized dissociation. We resolve this dispute by quantifying site-specific reactivity using a curved Pt single crystal surface. Reactivity is step type dependent and varies linearly with step density. Only the model that relies on localized dissociation is consistent with our results. Our approach provides absolute, site-specific reaction cross sections.**

At the heart of any chemical transformation lie the dynamical events associated with elementary reactions. In gas phase reactions, reactant energy is redistributed over the limited degrees of freedom available in the products. For gas-surface collisions, the bulk provides a massive sink for energy dissipation. This makes mechanistic problems for gas-surface reactions quite

challenging, as exemplified by ongoing discussion regarding the role of phonons and electron-hole pairs in surface reactions.(1, 2) In addition, surface heterogeneity may cause site-specific reactions to dominate overall kinetics in catalysis. For example, CO oxidation was recently shown to be site-specific on both Pt(3) and Pd(4).

The prototypical system in heterogeneous catalysis is H<sub>2</sub> dissociation on Pt. It is essential to the development of chemically accurate theoretical modeling of gas-surface interactions.(5) It is clear that H<sub>2</sub> dissociation occurs through dynamical processes.(5, 6) However, after four decades of research, two opposing dynamical models describing H<sub>2</sub> dissociation prevail in the literature. The fundamental discrepancy between the models lies in the assumed fate of kinetic energy of incident molecules. In the first model, it is conserved in the collision and incident molecules elastically scatter into a precursor state. In the second model, incident kinetic energy is not conserved. Depending on the exact point of impact, it couples directly to the dissociation coordinate or is dissipated, for example, by excitation of a frustrated rotation.

The two models for H<sub>2</sub> dissociation on Pt surfaces are illustrated in figure 1. Model 1, schematically shown in figure 1a, was proposed by Poelsema, Lenz, and Comsa.(7, 8) Scattering experiments have previously shown that atoms and molecules may diffract into a physisorbed state.(9, 10) In their model, the elastic collision only leads to dissociation when a H<sub>2</sub> molecule also encounters a defect during friction-free diffusion across the surface. The model is summarized by:



The rate constant for adsorption ( $k_{ads}$ ) depends on the probability to resonantly scatter into the physisorbed state ( $S_{0,nL}$ ). The rates at which physisorbed molecules desorb ( $k_{des}$ ) or encounter defects ( $k_{defect}$ ) depend on their velocity ( $\nu$ ), residence time ( $\tau$ ), and the average distance be-

tween defects ( $L_d$ ). The model predicts a dissociation probability on the clean surface,  $S_0$ :

$$S_0 \propto S_{0,nL} \left( 1 - e^{-\frac{L_d}{\nu\tau}} \right) \quad (2)$$

For large distances between defects, reactivity is rather sensitive to  $L_d$ . For short distances, i.e. higher defect densities, this sensitivity is lost. The transition occurs when the mean free path of the physisorbed molecule, i.e.  $\nu \cdot \tau$ , is comparable to the distance between defects.

In model 2, Baerends,(11) Hayden,(12) and Somorjai(13) propose parallel dynamical mechanisms for different surface sites, e.g. terraces and steps. None of these mechanisms contains a long-lived, diffusing precursor state. Dissociation is adequately represented as elementary:



The observed reactivity represents an average ( $k_{ave}$ ) from site-specific contributions. Terraces contribute by direct dissociation, as illustrated in figure 1b. Incident kinetic energy is used to surmount activation barriers that vary with exact location and molecular orientation. Steps contribute by the two mechanisms illustrated in figures 1c and 1d. The first occurs at the cusp and is responsible for the initial negative correlation of reactivity with incident kinetic energy ( $E_{kin}$ ). (12, 14) Dynamical calculations suggest that kinetic energy is converted to molecular rotation. Dissociation occurs when the dynamically trapped molecule senses the upper edge of the step. (11) The second contribution by steps is barrier-free dissociation at the upper edge. (11, 12, 14–16) Kinetic energy flows into the reaction coordinate and is quickly lost to the substrate. The reactivity constant in this model can be represented as the weighted average of site-specific reactivities,  $S_0^{site}$ ,

$$S_0 \propto \sum_{site} f^{site} \cdot S_0^{site} \quad (4)$$

In contrast to the previous one, this second model thus predicts a strictly linear relation between reactivity and the fractional occurrence of each type of reactive site,  $f^{site}$ . Whereas the first model

also did not discriminate between defects, this model does allow for varying contributions by, e.g., the A- and B-type step edges depicted in figure 1.

A new approach allows us to test both models on a single sample. The step density along a curved Pt surface has been shown to vary smoothly from 'defect free' (111) to highly stepped surfaces.(17) By combining a curved surface approach and supersonic molecular beam methods (18) with highly improved spatial resolution, we resolve that H<sub>2</sub> dissociation does not require physisorption and diffusion to defect sites. In addition, we quantify site-specific reactivities for both {100} (A-type) and {110} (B-type) step types.

A schematic illustration of the experiment is shown in figure 2a-e. Our Pt single crystal is a 31° section of a cylinder along the [10 $\bar{1}$ ] rotational axis. The (111) surface appears at the apex.(19) The macroscopic curvature of the crystal is a direct result of monatomic steps.(17) Consequently, the local surface structure on our crystal varies smoothly from Pt(533) via Pt(111) to Pt(553).(19) As both A- and B-type steps are spatially separated by the (111) surface, their influence on reactivity can be probed independently. We measure initial sticking probabilities ( $S_0$ ) using the King and Wells approach.(20) The molecular beam is incident on the surface along the [111] vector. We measure  $S_0$  as a function of step density by translating the single crystal surface with respect to our rectangular-shaped supersonic molecular beam (0.126 x 6.0 mm<sup>2</sup>). Figure 2d illustrates the relative sizes of the crystal and the beam. Figure 2e quantifies the convolution of the narrow molecular beam with step density. Near (111) it is limited to 0.01 nm<sup>-1</sup>. Our measurements are limited to step densities of 0.8 nm<sup>-1</sup> due to narrowing of the crystal at high step densities in combination with the 6 mm width of our beam.

Figure 2f shows  $S_0$  at a surface temperature ( $T_s$ ) of 155 K as a function of step density and step type for  $E_{kin} = 9.3$  meV and 100 meV. These energies are produced by (anti)seeding

D<sub>2</sub> beams and estimated from time of flight measurements. At the lower  $E_{kin}$ ,  $S_0$  starts at  $0.01 \pm 0.05$  for the (111) surface and increases linearly with step density.  $S_0$  for B-type step edges are consistently higher than A-type step edges at similar step density. At the higher  $E_{kin}$ , the influence of steps has disappeared and  $S_0$  is approximately constant over the entire step density range. This energy dependence is consistent with all previous King and Wells studies of H<sub>2</sub> dissociation on flat and stepped single crystal surfaces. (12, 14–16, 21, 22)

For the lower  $E_{kin}$ , where steps are the dominant source of dissociation, figure 3 compares  $S_0$  as a function of step density for  $T_s = 155$  K and 300 K. Results are only shown for B-type steps, but the trend is identical for A-type steps. Also shown as dashed lines are predictions for  $S_0$  by model 1,(8) as described in the supporting materials. The curvature in the predicted step density dependence is a logical consequence of model 1. When the 'mean free path' of the physisorbed state approaches or exceeds the distance between defects, increasing defect density becomes less effective in increasing  $S_0$ . Only at high defect density, does  $S_0$  become proportional to step density.

Our results are clearly at odds with the predictions by this model. Not only is  $S_0$  underestimated over the entire defect density range, two crucial dependencies are not reproduced in the experiment. First, predicted curvature in the  $S_0$  dependence on step density near the (111) surface is absent. Second, the  $T_s$  dependence opposes the predicted trend. Whereas model 1 clearly reduces  $S_0$  with increasing  $T_s$  due to the diminishing residence time in a physisorbed state, we find that  $S_0$  generally increases or is hardly affected. An attempt to improve the model by incorporating Debye-Waller attenuation, reducing the probability of scattering into the resonant state, would increase this discrepancy. In addition to these erroneous dependencies, the site specific reactivity of  $S_0$  seen in figure 2f is not captured in model 1. Finally, it also does not capture the observed step density independence at the higher  $E_{kin}$ .

In contrast, our results are in agreement with the two underlying assumptions of model 2. Terrace and step sites contributing proportionally to their abundance and the absence of a freely diffusing precursor require a strictly linear dependence of  $S_0$  on step density. Least squares fitting yields a residual reactivity due to dissociation on the Pt(111) surface. Individual fits to A and B-type steps for lower incident energy yields  $0.023 \pm 0.009$  and  $0.040 \pm 0.008$ . This is in good agreement with previous results(21, 22) for Pt(111), even with experimental results for the clean 'defect free' surface (7) on which model 1 is based. This residual reactivity of the 'defect free' Pt(111) surface is explained by recent dynamical calculations for D<sub>2</sub> dissociation.(23) Select impact geometries show barrier-free dissociation on the Pt(111) surface.

The slope of the linear fits in figure 2f reflect the summed contributions of direct barrier-free and trapping-mediated dissociation at step edges, shown in figures 1c-d. Multiplying the slope of each linear fit with the width of the unit cell yields the reaction cross section for H<sub>2</sub> dissociation at the step edge.(16) For our low  $E_{kin}$  data at  $T_s = 155$  K, these are  $0.108 \pm 0.007$  and  $0.157 \pm 0.007$  nm<sup>2</sup> for A- and B-type steps. The reaction cross section for A-type steps agrees quantitatively with theoretical results that show the surface area of the Pt(211) unit cell where impact at the step results in dissociation.(11) We previously showed that the direct contribution at the upper edge, shown in figure 1d, amounts to  $0.043$  nm<sup>2</sup>.(16) The trapping-mediated mechanism in figure 1c is then responsible for the  $0.065$  nm<sup>2</sup> difference at A-type steps. As the local structure at the upper edge is identical, the significantly larger cross section for B-type steps compared to A-type steps suggests larger and/or deeper molecular chemisorption wells at its cusp.

In summary, the model ascribing H<sub>2</sub> dissociation on Pt mostly to a highly mobile precursor fails to predict the reactivity dependence on step density and surface temperature. In addition to a lack of site specificity, the model erroneously assumes that the perfect Pt(111) surface only

exhibits activated adsorption.<sup>(23)</sup> As reactivity in this model is fully ascribed to defects, the model's parameters and other conjectures must reflect this overestimate. We believe this to be represented by the unphysical assumption that all scattering occurs into the ground vibrational level of the physisorbed state. Furthermore, while the model's parameters are based on a fit to experimental data using dissociation from a bulb gas at room temperature, the known complex angular dependence to dissociation (21, 24) is not taken into account. More assumptions may contribute to its failure, e.g. that no other possible outcome than dissociation exists when physisorbed molecules encounter a defect.

Simultaneously, our data support that dissociation is dominated by impulsive interactions at the impact site. In the relevant regime, there is no significant surface temperature dependence and, at low kinetic energy, dissociation is strictly linear with step density. At incident energies exceeding most barriers to dissociation on the terrace, the contribution of steps becomes indiscernible; reactivity becomes independent of step density. From our low kinetic energy data, we extract site specific reaction cross sections for A- and B-type step edges in a chemical reaction. The reaction cross section of B-type steps is significantly larger than that of A-type steps, suggesting a larger molecular chemisorption well with more efficient kinetic energy dissipation. These results present benchmarks for future construction of high dimensional potential energy surfaces and guide dynamical studies aiming to understand the kinetics of this prototypical system. In particular, the origin of the significantly larger cross section for dissociation at B-type step edges may be extracted from calculation of the potential energy surface of H<sub>2</sub>/Pt(221). Additional (quantum) dynamical calculations, similar to those performed by Baerends and coworkers<sup>(11, 25)</sup> could confirm the dominant contributions of the three parallel dynamical mechanisms captured by model 2.

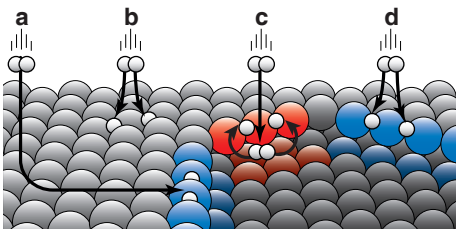


Figure 1: a) Model 1: mobile precursor mechanism. b) Model 2: direct activated dissociation at (111) terraces. c) Model 2: trapping mediated dissociation at step edges. d) Model 2: direct dissociation at step edges. A- and B-type steps are shown in blue and red respectively. c) and d) can take place at either step type but relative contributions may vary.

## References

- [1] B. Gergen, H. Nienhaus, W. H. Weinberg, E. W. McFarland, *Science* **294**, 2521 (2001).
- [2] J. Meyer, K. Reuter, *Angew. Chemie Int. Ed.* **53**, 4721 (2014).
- [3] J. Neugeboren, *et al.*, *Nature* **558**, 280 (2018).
- [4] S. Blomberg, *et al.*, *ACS Catalysis* **7**, 110 (2017).
- [5] G. J. Kroes, *Science* **321**, 794 (2008).
- [6] C. Diaz, *et al.*, *Science* **326**, 832 (2009).
- [7] B. Poelsema, K. Lenz, G. Comsa, *J. Phys. Condens. Matter* **22**, 304006 (2010).
- [8] B. Poelsema, K. Lenz, G. Comsa, *J. Chem. Phys.* **134**, 074703 (2011).
- [9] J. P. Cowin, C.-F. Yu, S. J. Sibener, L. Wharton, *J. Chem. Phys.* **79**, 3537 (1983).
- [10] A. S. Sanz, S. Miret-Artés, *Phys. Rep.* **451**, 37 (2007).
- [11] D. A. McCormack, R. A. Olsen, E. J. Baerends, *J. Chem. Phys.* **122**, 1 (2005).
- [12] A. T. Gee, B. E. Hayden, C. Mormiche, T. S. Nunnery, *J. Chem. Phys.* **112**, 7660 (2000).



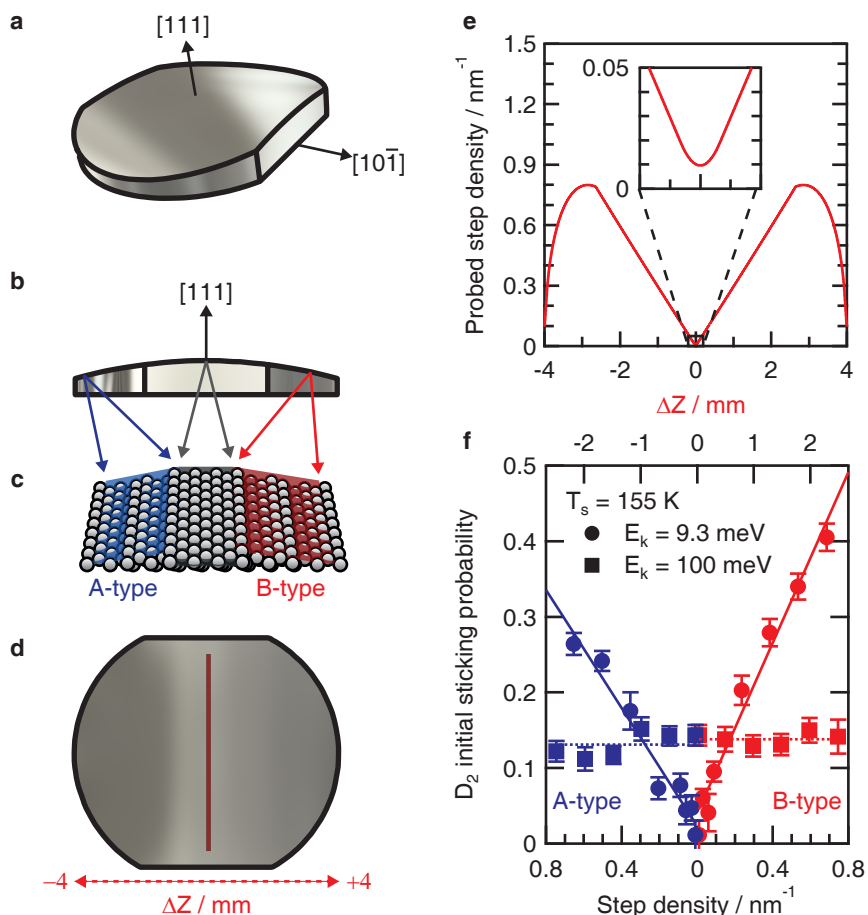


Figure 2: a) Birdseye view of the curved Pt single crystal. b) Side view along the  $[10\bar{1}]$  vector. c) Side view showing the surface structure and surface planes of Pt(533) (A-type steps), Pt(111), and Pt(553) (B-type steps) in blue, gray, and red, respectively. d) Top view with the molecular beam size in red. e) Step density probed by the molecular beam at the position relative to the (111) surface. f)  $S_0$  ( $D_2$ ) at  $T_s = 155 \text{ K}$  as a function of step density. Results from A and B-type step edges are depicted in blue and red. Circles and squares represent  $E_{kin} = 9.3 \text{ meV}$  and  $E_{kin} = 100 \text{ meV}$ . Lines are least square fits to the data. Error bars represent the standard deviation in  $S_0$ .

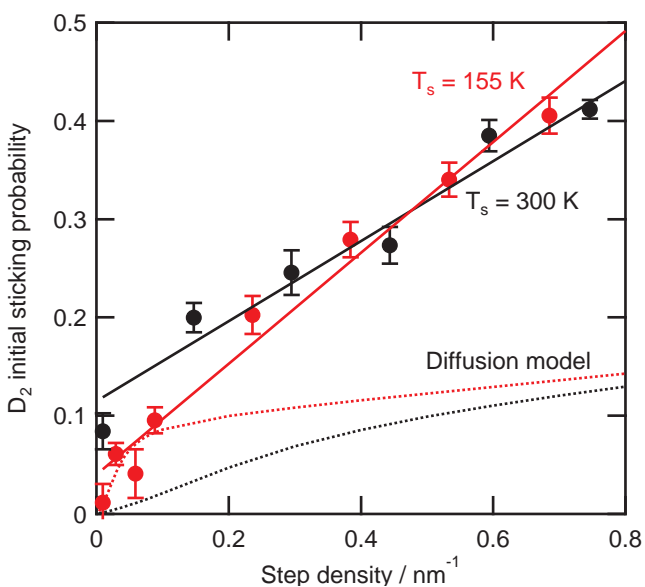


Figure 3:  $S_0(D_2)$  for  $E_{kin} = 9.3$  meV as a function of B-type step density. Circles are measured data. Solid lines are fits to the data. Dashed lines are predicted results from model 1. Red and black represent  $T_s = 155$  K and 300 K respectively. Error bars represent the standard deviation in  $S_0$ .

- [13] M. Salmeron, R. J. Gale, G. A. Somorjai, *J. Chem. Phys.* **67**, 5324 (1977).
- [14] I. M. N. Groot, K. J. P. Schouten, A. W. Kleyn, L. B. F. Juurlink, *J. Chem. Phys.* **129**, 224707 (2008).
- [15] I. M. N. Groot, A. W. Kleyn, L. B. F. Juurlink, *Angew. Chemie Int. Ed.* **50**, 5174 (2011).
- [16] I. M. N. Groot, A. W. Kleyn, L. B. F. Juurlink, *J. Phys. Chem. C* **117**, 9266 (2013).
- [17] A. L. Walter, *et al.*, *Nat. Commun.* **6**, 8903 (2015).
- [18] C. Hahn, *et al.*, *J. Chem. Phys.* **136** (2012).
- [19] A. J. Walsh, *et al.*, *J. Vac. Sci. Technol. A* **35**, 03E102 (2017).
- [20] D. A. King, M. G. Wells, *Surf. Sci.* **29**, 454 (1972).

- [21] A. C. Luntz, J. K. Brown, M. D. Williams, *J. Chem. Phys.* **93**, 5240 (1990).
- [22] P. Samson, A. Nesbitt, B. E. Koel, A. Hodgson, *J. Chem. Phys.* **109**, 3255 (1998).
- [23] E. Nour Ghassemi, M. Wijzenbroek, M. F. Somers, G. J. Kroes, *Chem. Phys. Lett.* **683**, 329 (2017).
- [24] K. Cao, R. van Lent, A. W. Kleyn, L. B. F. Juurlink, *Chem, Phys. Lett.* **706**, 680 (2018).
- [25] M. Luppi, D. A. McCormack, R. A. Olsen, E. J. Baerends, *J. Chem. Phys.* **123**, 164702 (2005).
- [26] D. J. Auerbach, in *Atomic Molecular Beam Methods*, G. Scoles, ed. (Oxford Univ. Press, Oxford, 1988), chap. 14, pp. 362–379.
- [27] G. Füchsel, *et al.*, *J. Phys. Chem. Lett.* **9**, 170 (2018).

**Acknowledgements:** The authors thank T. Hoogenboom and P.J. van Veldhuizen for technical support. **Funding:** This work is part of the CO<sub>2</sub> neutral fuels research program, which is financed by the Netherlands Organization of Scientific Research (NWO). **Author contributions:** All the authors contributed substantially to this work. **Competing interests:** The authors declare no competing interests. **Data and materials availability:** All data supporting the conclusions are available in the published work or supporting materials.

Supporting materials:

- Experimental details
- Supersonic molecular beam characterization
- Initial sticking probability
- Predicted initial sticking probabilities by model 1

References only in SM: (See list of references above.)

- [26] D. J. Auerbach, in *Atomic Molecular Beam Methods*, G. Scoles, ed. (Oxford Univ. Press, Oxford, 1988), chap. 14, pp. 362379.
- [27] G. Fuchsel, et al., *J. Phys. Chem. Lett.* 9, 170 (2018).

## 1 Supplementary Materials

All experiments were performed in a homebuilt supersonic molecular beam ultra-high vacuum (UHV) apparatus. The base pressure of the UHV chamber is  $<1 \cdot 10^{-10}$  mbar. The UHV chamber contains, amongst others, low energy electron diffraction (LEED) / Auger electron spectroscopy (AES) optics (BLD800IR, OCI Vacuum Microengineering), a quadrupole mass spectrometer (QME200, Pfeiffer vacuum) for residual gas analysis and King and Wells (KW) measurements, and an on-axis quadrupole mass spectrometer (UTI-100C) for time-of-flight (TOF) measurements.

The UHV chamber holds our curved Pt single crystal (Surface Preparation Lab). It is cooled using a liquid nitrogen cryostat and heated through radiative heating and electron bombardment using a filament. The Pt single crystal was cleaned with repeated cycles of sputtering ( $6 \cdot 10^{-6}$  mbar Ar, Messer 5.0, 0.5 kV,  $1.3 \mu\text{A}$ , 910 K,  $50^\circ$ , 5 min), oxidation ( $3.5 \cdot 10^{-8}$  mbar O<sub>2</sub>, Messer 5.0, 910 K), and *in vacuo* annealing (1200 K). For the final cleaning cycle, the Pt crystal is only sputtered and annealed at 910 K. Surface quality was verified using LEED and AES.

The double differentially pumped supersonic beam of D<sub>2</sub> is formed by expanding a gas mixture from a W nozzle with a 28  $\mu\text{m}$  orifice. The center of the expansion is selected using a skimmer. A second skimmer and a sliding valve with different orifices create the molecular beam of variable size and shape within the UHV chamber. For the measurements, we use a slit as the defining orifice in the sliding valve. The molecular beam can be modulated by a mechanical chopper for time of flight spectroscopy or a pair of flags for King and Wells measurements. The kinetic energy ( $E_{kin}$ ) of the D<sub>2</sub> beam is varied by seeding in H<sub>2</sub> or anti-seeding in Ar. TOF spectra are measured at 6 different on-axis mass spectrometer positions. The resulting TOF

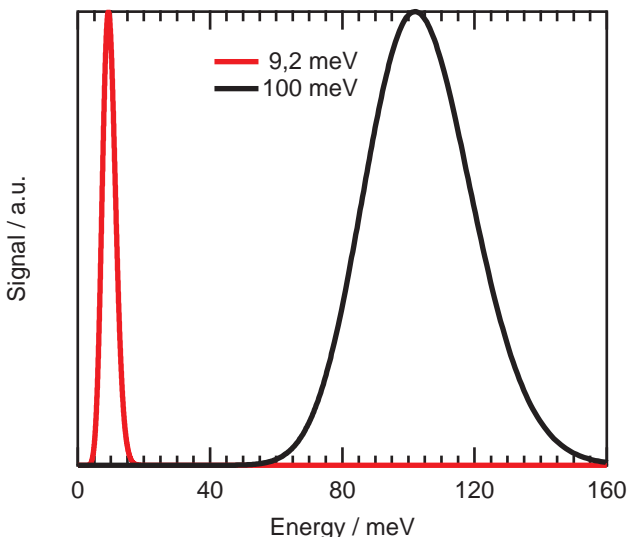


Figure 4: Fitted energy distributions for the D<sub>2</sub> beams used.

spectra are fitted with the functional form for a density-sensitive detector:(26)

$$f(t) = \left(\frac{l}{t}\right)^4 \cdot e^{-\left(\frac{t-t_0}{\alpha}\right)^2} \quad (5)$$

where  $l$  is the neutral flight path,  $t$  is the neutral flight time,  $t_0$  is the stream flight time and  $\alpha$  is the width of the distribution. There are several offsets between the measured time and the actual neutral flight time. To determine the total offset,  $t_{offset}$ , TOF spectra are measured at 6 different QMS positions and fitted with a Gaussian function. We use linear regression on the resulting peak positions to extrapolate to  $l = 0$  to extract  $t = t_{offset}$ . We subtract  $t_{offset}$  from the measured time, leaving only the neutral flight time  $t$  expressed in equation 5. The TOF spectra are subsequently fitted with equation 5. After redimensioning the fits using the appropriate Jacobian for transformation,(26) we obtain the two energy distributions in figure 4.

D<sub>2</sub> initial sticking probabilities are measured using the standard King and Wells (KW) method.(20) The flags are controlled using a Labview program to ensure that the time delay between opening and closing the two flags is well-defined. The resulting measured sticking curves are highly

reproducible. Therefore, we can use signal averaging of multiple measurements to increase signal-to-noise levels.(27) We measure sticking curves at up to 8 different crystal positions (surface structures) consecutively in one experiment. After each experiment with 7 or 8 surface structures probed, we flash the crystal to 550 K to desorb all D<sub>2</sub>. We perform a sputter and anneal cycle after 8 experiments.

Sticking on surfaces with low step density show the strongest time (coverage) dependence. Consequently, we start every sticking experiment at or nearest to the (111) apex and expose the crystal to the D<sub>2</sub> beam for only 3 s at each position. We probe different surface structures on the crystal by moving the crystal with respect to the beam, starting from the apex, in one direction in increments of 1 mm. In this way, we measure sticking probabilities for a number of relative crystal positions (and different surface structures) in one experiment, e.g. 0 mm (111), +1 mm, +2 mm, +3 mm, -3 mm, -2 mm, -1 mm. Consecutive experiments are performed in reverse order, but still start at or close to the (111) surface. We observe no difference in S<sub>0</sub> between experiments performed in normal or reverse order.

Two typical KW traces for surfaces containing A- or B-type step edges are shown in figure 5 along with the fits used to extrapolate to S<sub>0</sub>. S<sub>0</sub> is extracted from these time (coverage) dependent data by extrapolating a linear least squares fit to t = 0 s:

$$S(t) = S_0 + \frac{dS}{dt} \cdot t \quad (6)$$

There is an error in S<sub>0</sub> due to an uncertainty in the slope and the intercept. An additional error is introduced in t = 0, because the mass spectrometer measures ~ 7 data per second. We assume that the flag, and hence S<sub>0</sub>, occurs at t = 0 s. We calculate the error propagation in the usual way for multiplication and summation.

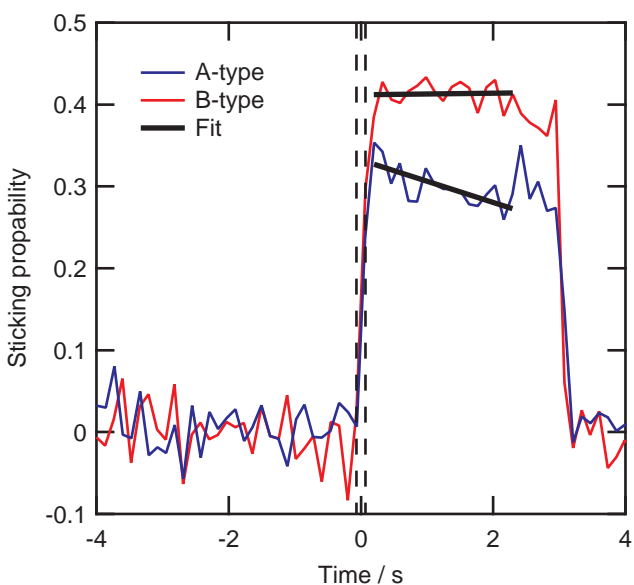


Figure 5: Typical signal averaged King and Wells traces are shown in blue and red for A- and B-type step edges. The black linear fit is extrapolated to  $t = 0$ . The dashed lines indicate the error in determining  $t = 0$ .

The predictions by model 1 shown in figure 3 for the zero coverage limit are calculated by:

$$\tau = \frac{h}{k_B T_s} e^{\left(\frac{\eta E_W}{k_B T_s}\right)} \quad (7)$$

$$S_0 = S_{0nL} \frac{\nu\tau}{L_d} \left(1 - e^{\left(-\frac{L_d}{\nu\tau}\right)}\right) + 0.24\theta_d \quad (8)$$

The residence time  $\tau$  depends on the precursor well depth  $E_W$ , and  $T_s$ .  $S_0$  is the summation of two terms. The first term multiplies the probability of capture into the physisorbed state ( $S_{0nL}$ ) with the probability of reaching a defect. The latter probability depends on  $\tau$ , the incident velocity ( $\nu$ ), and the average distance between defects ( $L_d$ ). The second term quantifies a minor contribution, i.e. the probability of dissociation through direct impact on defects. It equals 0.24 times the fractional defect density ( $\theta_d$ ), which can be converted to step density in  $\text{nm}^{-1}$  by dividing by the Pt-Pt distance: 0.277 nm.<sup>(8)</sup> Besides Planck's constant ( $h$ ), and Boltzmann's constant ( $k_B$ ), the model requires an additional fit parameter ( $\eta$ ) and assumes a  $\theta_d$  dependence for  $E_W$ .<sup>(8)</sup>